Locally Competitive Coordination Electrolyte for High-Voltage Lithium-Metal Batteries with Ni-Rich Cathodes

Jianqi Sun [a,], Juliane Fiates [b,e], Kohei Shimokawa [a], Qingsong Weng [a], Heng Wang [a], Zhuangnan Li [c], Su Jin Heo [a], Hooman Abbasi [a], Minfei Fei [a], Tianhao Wu [c], Yaogang Li [d], Hongzhi Wang [d], James A Dawson [b,e], Michael De Volder [a,e]**

a. Jianqi Sun, Kohei Shimokawa, Qingsong Weng, Heng Wang, Sujin Heo, Hooman Abbasi, Minfei Fei, Michael De Volder
Department of Engineering, University of Cambridge, Cambridge, United Kingdom
E-mail: js2677@cam.ac.uk; mfld2@cam.ac.uk

b. Juliane Fiates, James Dawson
Chemistry-School of Natural and Environmental Sciences, Newcastle University, Newcastle upon Tyne, United Kingdom

c. Zhuangnan Li, Tianhao Wu
Department of Materials Science and Metallurgy, University of Cambridge, Cambridge, United Kingdom

d. Yaogang Li, Hongzhi Wang
College of Materials Science and Engineering, Donghua University, Shanghai, P. R. China

e. Juliane Fiates, James Dawson, Michael De Volder
The Faraday Institution, Quad One, Harwell Science and Innovation Campus, Didcot OX11 0RA, United Kingdom

Funding: European Research Council (ERC) Consolidator Grant (MIGHTY 866005), Faraday Institution (Degradation FIRG024, FIRG060, FIRG019).

Keywords: lithium batteries, solvation structure engineering, electrode-electrolyte interphase, anode-free batteries, nickel-rich cathode

Abstract

Lithium (Li) metal anodes (LMAs) hold great promise to increase the energy density of batteries. This is especially true when using an energy dense cathode such as Ni-rich layered transition metal oxides, but unfortunately, these lead to accelerated capacity loss when combined with LMAs. Ni-rich cathodes suffer from surface reduction, which can be accelerated in contact with certain electrolyte solvents. This in turn leads to transition metal dissolution and shuttling, which poisons the solid electrolyte interphase (SEI) and complicates the anode stabilization. Here, we propose nitrile primary solvent combined with ether co-solvent, diluent and two borate salts to suppress parasitic reaction. A competition in the ion coordination between solvents surrounded by diluents is achieved. This leads to the anions being preferentially decomposed in the SEI and enhanced reversibility. Using high cathode areal capacity (4.0 mAh cm^{-2}), thin LMAs (N/P=2.5), lean electrolyte (3 g Ah^{-1}), and high charging voltages (≥4.4 V), we achieve a capacity retention of 80% over 250 cycles. With moderately high loading cathode (3.4 mAh cm^{-2}) but higher upper voltage (4.6 V), the cells retain 87.5% capacity retention over 430 cycles. Finally, we demonstrate Ah-level anode-free pouch cells with a 78.7% capacity retention over 100 cycles.

1. Introduction

Lithium-ion batteries (LIB) have emerged as the dominant electrochemical energy storage technology due to their ability to meet the high energy density requirements of portable electronic devices and electric vehicles.[1-3] However, emerging applications such as autonomous robots and electric aircrafts require energy densities pushing beyond the limits of current LIB technology.[4, 5] Li metal offers the highest anode specific capacity (3860 mAh g^{-1}) and the lowest electrochemical potential (− 3.04 V vs. standard hydrogen electrode).[6, 7] When paired with nickel-rich layered oxide cathodes, such as $LiNi_{0.8}Mn_{0.1}Co_{0.1}O_2$ (NMC811), lithium metal batteries (LMBs) have the potential to break through the current 500 Wh kg^{-1} ceiling.[8, 9]

Further, to achieve high energy densities, the cell needs to employ a high areal capacity (e.g., ≥4 mAh cm^{-2}), a low N/P ratio, and high upper cutoff voltage, but these requirements tend to exacerbate the aforementioned issues with rapid capacity loss.[10, 11] Overcoming these degradation issues necessitates a range of measures, of which the development of innovative electrolytes has received the most attention. In a classic electrolyte design, carbonate solvents with high polarity such as ethylene carbonate (EC) are used to facilitate Li salt dissociation as well as the stable operation of the graphite anode. However, these electrolytes show poor capacity retention when used in combination with LMAs.[12, 13] In addition, it has been shown that EC can lead to accelerated reduction of the NMC811 cathode surface (**Figure 1**), which in turn leads to transition metal (TM) dissolution which further affects the stability of the solid electrolyte interphase (SEI) and exacerbates Li-inventory loss.[14-16] Many advancements have been made in changing the electrolyte formulation for stabilizing Li plating and stripping, such as localized high concentration electrolyte (LHCE),[17-19] and weakly solvated electrolytes,[20-22] but perhaps insufficient attention has been given to the interaction of these electrolytes with the cathode. To address this, in this paper, we start from a combination of succinonitrile (SN) and fluoroethylene carbonate (FEC) which show good stability against oxidation and reduce oxygen loss from the cathode surface and the TM dissolution process that are linked with this.[23] Further, their high polarities enable them to better dissociate borate salts (LiDFOB and LiBOB).[24, 25] Increasing the salt concentration lowers the probability of free solvent molecules being reduced by LMA and increases anion contribution to SEI construction, which tends to extend the battery lifespan. However, high salt concentrations render electrolyte too viscous and economically unfeasible. We therefore adopt 1,1,2,2-tetrafluoroethyl-2,2,3,3-tetrafluoropropyl ether (TTE) as a diluent, but observed that it shows phase-separation with the above electrolyte. We found that 1,2-dimethoxyethane (DME) helps bridging these solvents,

which completes our electrolyte design (Figure S1). Spectral analysis combined with molecular dynamics simulation also proves that DME's strong solvating capability (higher donor number) allows it to participate in the primary solvation and weaken the Li^+–SN interaction, contributing to a diverse Li^+ solvation environment. Ultimately, Li^+-anion coordination is found to be increased by competitive coordination between DME and SN, as well as the intermolecular hydrogen bonding and dipole interactions between TTE and the primary solvents.

Overall, the proposed locally competitive coordination electrolyte (LCCE) design strikes a balance between suppressing NMC811degradation and Li plating and stripping reversibility (Figure 1). Even when using high areal capacity electrodes (~4 mAh cm^{-2}), an N/P ratio of 2.5, and a high charge cutoff voltage of 4.4 V, LMBs utilizing the proposed electrolyte achieve 80% capacity retention over 250 cycles, whereas reference carbonate-based electrolytes and 1,2-dimethoxyethane based-locally concentrated electrolytes achieve only 49 and 117 cycles respectively under the same conditions. At a higher upper cutoff voltage (4.6 V), LCCE still enables LMBs to retain outstanding capacity retention (87.5%) over 430 cycles even with moderately high loading cathode (~3.4 mAh cm^{-2}). Finally, the anode-free pouch cell with the designed electrolyte delivered 1.074 Ah at 0.5 C and maintained ~78.7% capacity retention over 100 cycles.

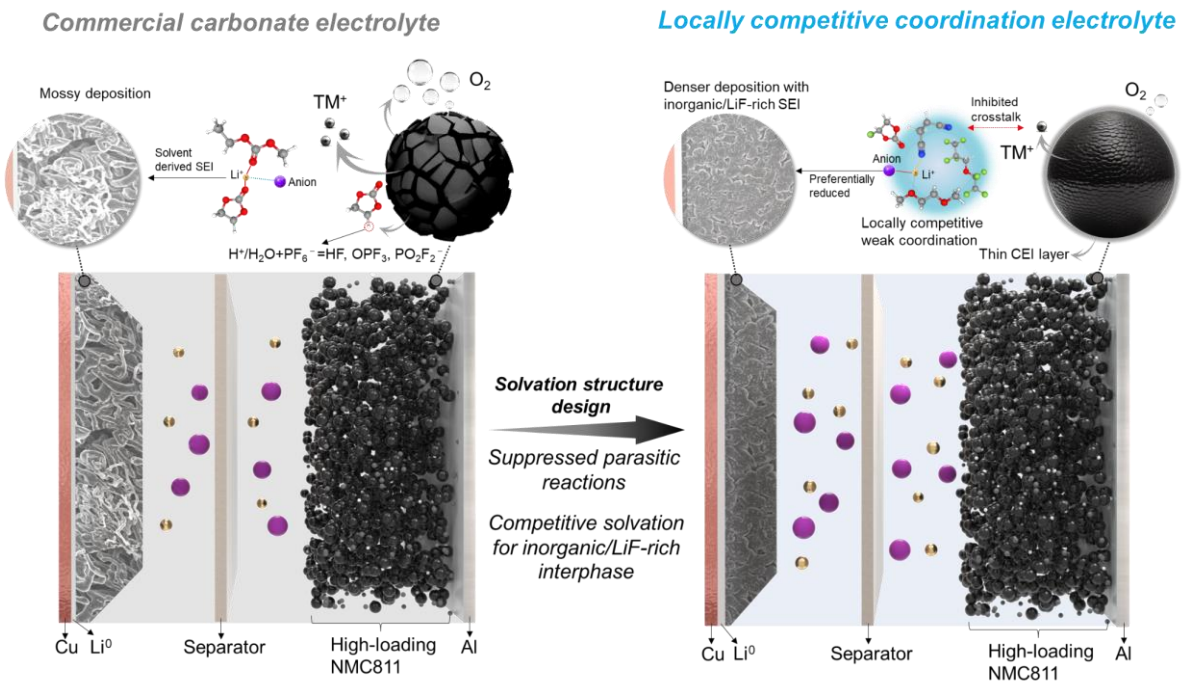


Figure 1. Schematic illustration comparing LCCE with typical carbonate electrolytes on improving electrode compatibility and cycling performance.

2. Results and Discussion

As mentioned above, the first objective of this work is to develop electrolytes that not only focus on LMA stability, but also compatibility with NMC811 cathodes. For the latter, we employ both salts and solvents that have high resistance against oxidation and reduce cathode oxygen loss. First, we propose a dual-salt strategy of LiDFOB and LiBOB in our electrolytes, because they are preferentially oxidized for contributing to the inhibition of aluminum corrosion and the rapid formation of protective interphases on the electrodes.[26-28] Due to their weak charge delocalization, achieving salt dissociation at elevated salt concentrations relies on overcoming high cation-anion binding energy.[29, 30] To achieve this, we combine SN and FEC solvents which have high dielectric constants and dipole moments (**Figure 2**a). Although FEC can be reduced for interphase in priority to mitigate the extent to which the cyano moieties of SN are reduced by LMA, [31] during prolonged cycling, the loss of SEI integrity can still potentially allow SN to come into contact with the LMA, especially under lean LMA conditions. Increasing the salt concentration can reduce the proportion of free SN but increase anion contribution to SEI construction, thereby lowering the probability of SN reduction by LMA. However, it should be noted that a strong dissociation capability does not necessarily imply a better dissolution of salt. A higher salt concentration would markedly increase the viscosity of the SN/FEC electrolyte and aggravate cell polarization. We seek to address that using TTE diluent, which has low dielectric constant, donor number, and weak polarity. These characteristics also drive TTE as the secondary solvation sheath encapsulating the SN-solvated clusters, suppressing the exposure of the α-hydrogens of SN through dipole interactions with fluorine, enhancing electrolyte long-term compatibility with LMA. The spatial distribution of TTE around SN (derived from molecular dynamics, Figure S2) indicates that the TTE may partially shield the nitrogen site from Li^+ coordination and reduce its susceptibility to reduction. Unfortunately, during the electrolyte formulation, we observed that the SN/FEC (9:1 by volume) electrolytes show a limited miscibility with TTE (Figure S3). This structural arrangement may impose an obstacle to the quick de-solvation.

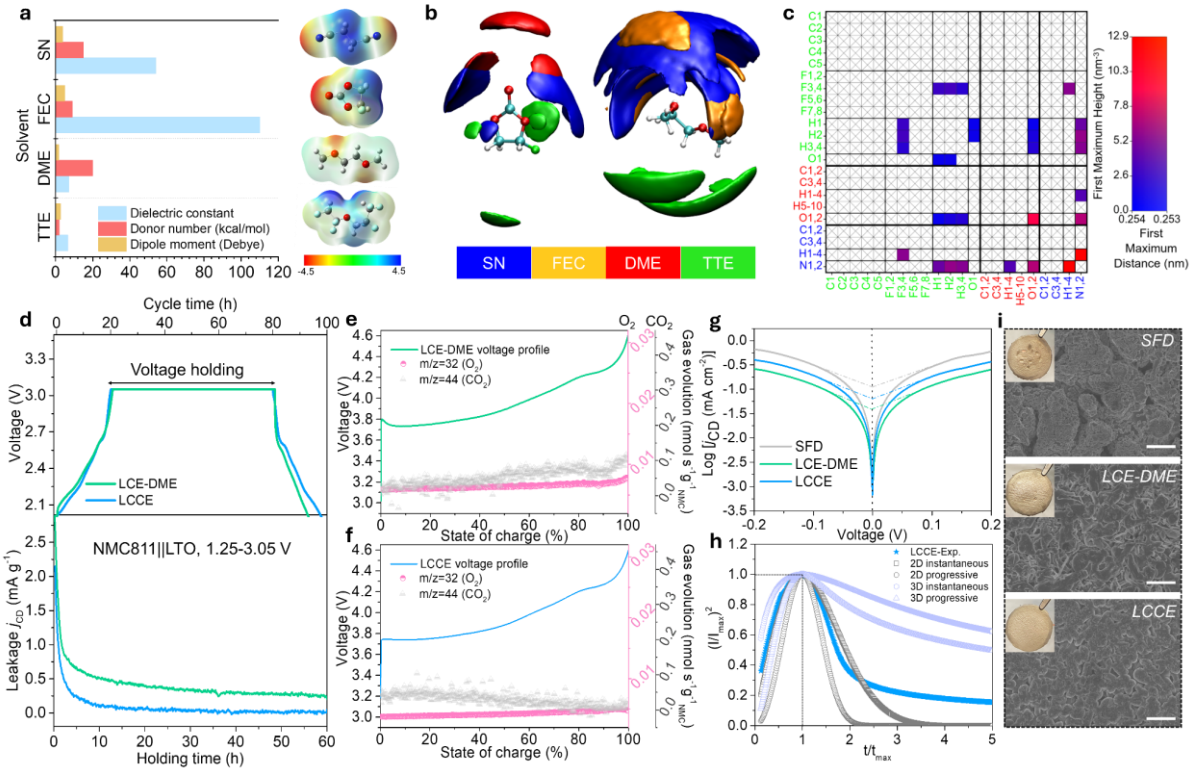


Figure 2. (a) Dielectric constants, donor numbers, dipole moments, and electrostatic potential maps of solvents and diluents in LCCE. (b) Spatial distribution function analysis of solvent/diluent interactions in LCCE. (c) Hydrogen-bond network among SN (dark blue), DME (red), and TTE (green). (d) Voltage holding test of LCE-DME and LCCE normalized to the mass loading of NMC811. Gas evolution from NMC811//Li cells using (e) LCE-DME and (f) LCCE electrolytes based on in situ DEMS analysis. (g) Tafel plots of different electrolytes. (h) Dimensionless nucleation curves for Li deposition in LCCE. (i) SEM images of deposited Li (on Cu, 0.5 mA cm^{-2}, 5 mAh cm^{-2}) via different electrolytes, scale bar 10 μm.

To overcome this, we found that DME shows decent amphiphilicity between SN, FEC, and TTE. acting as a bridge between these components. Together with its higher donor number, DME also coordinates with Li^+ in the primary solvation shell, which reduces the Li^+ de-solvation energy compared to electrolytes using SN only. DME's dual role in this electrolyte design is the key to achieve an overall enhanced performance. To shed light on the dual polar-philic/phobic DME role in our electrolyte, we computed the spatial distribution function (SDF) (Figure 2b) and the hydrogen bond network map (Figure 2c) from molecular dynamics (MD) simulations. These results show that DME tends to strongly interact with both TTE and SN, denoted by the increased concentration of them surrounding DME when compared to FEC. This corroborates the experimental observation above of better solubility of TTE in the presence of DME. In the hydrogen bond network map, the first maximum heights quantify the propensity

or strength of hydrogen bonding for a specific atomic pair at their characteristic bonding distance.[32] The interactions between DME, SN, and TTE, involve the ether oxygen (EO) atoms (O1,2) in DME acting as hydrogen bond acceptors (Figure S4), forming intermolecular hydrogen bonds with either the α-hydrogens (connected with cyano moieties) of SN or the hydrogens of fluorinated moieties in the TTE. Similarly, the N of cyano moieties in SN serve as hydrogen bond acceptors, interacting with the α-hydrogens of EO bonds and the hydrogen atoms of TTE fluorinated groups. The dual interaction of DME with SN and TTE, provides a bridge for the formation of hydrogen bonds between SN and TTE make them miscible (Figure S3). Our radial distribution function (RDF) results show that bonding sites in SN are predominantly occupied by Li^+ and anions in the presence of high concentrations of salts (Figure S5), thereby inhibiting the mutual solubility between SN electrolytes and TTE. But after adding DME, the coordination between DME and SN may help release part of their bonding sites, allowing SN to interact with TTE through intermolecular hydrogen bonds. This indicates that even in the outermost Li^+ solvation shell, TTE may still influence the solvation strength experienced by SN in the inner solvation layer.

Next, we experimentally evaluate the influence of different ratios of TTE (as demonstrated in Figure S6) within LCCE through the battery's capacity retention. A solvent-to-diluent volume ratio of 0.75 (molar ratio of 1.31) (that is LCCE4) yields the highest capacity retention, establishing the baseline formulation for subsequent discussions and tests unless otherwise specified. For comparison, a diluent-free LCCE (SN/FEC/DME as solvents, denoted as SFD) and a DME-based locally concentrated electrolyte (DME/TTE as solvents, denoted as LCE-DME) with equal solvent-to-diluent volume ratios were made as reference electrolytes (see more details in Table S1).

Next, voltage hold and leakage current analysis are used to compare the surface reactivity of the NMC811 in different electrolytes. At an upper cutoff of 4.4 V (corresponding to 2.85 V in case of NMC811// $Li_4Ti_5O_{12}$ (LTO), see Figure S7), SFD, LCE-DME, and LCCE all exhibit lower leakage currents than a standard carbonate solvent electrolyte (LP57/VC), implying reduced parasitic reaction by the proposed electrolytes.[33, 34] Further, LCE-DME and LCCE exhibit lower average leakage currents than SFD during the last 20 h. To accentuate cathode degradation, we repeat the voltage hold experiment with an upper cutoff voltage of 4.6 V. Here LCCE clearly show reduced parasitic currents than LCE-DME (Figure 2d), which is in part due to SN's stability against oxidation (Figure S8 and S9). Then, we perform in situ differential electrochemical mass spectrometry (DEMS) to see the quantification of gas evolution from cells with different electrolytes (Figure 2e and f, Figure S10). With an upper cutoff voltage of

4.6 V, the cell with LP57/VC electrolyte shows evident gas evolution at high state of charge, indicating the severe parasitic reaction between electrolyte and cathode. The LCE-DME and LCCE enable the suppressed gas evolution compared to LP57/VC, moreover in particular, the oxygen release is suppressed more obviously in LCCE. These results provide direct evidence for that the LCCE exhibits less parasitic reaction and consequential better compatibility with Ni-rich cathodes.

Next, we verify the compatibility of the electrolytes with LMA via a modified Aurbach protocol in Li//Cu cells (Figure S11). This protocol mainly consists of one formation cycle for Li plating and stripping, and then repeatedly plating/stripping Li after pre-plating a Li reservoir on Cu with fixed capacity, the final all stripped Li capacity is used to determine the coulombic efficiency (CE). This analysis shows average Aurbach CEs of 91.9%, 96.7%, and 97.2% for SFD, LCE-DME, and LCCE respectively. These values align with initial cycling experiments in same configured half-cells (Figure S12), indicating that LCCE enhances Li plating/stripping reversibility.

Tafel plots of Li//Li symmetric cells demonstrate that SFD exhibits the highest exchange current density (2.81 mA cm^{-2}), signifying rapid charge-transfer kinetics (Figure 2g).[35] However, scanning electron microscopy (SEM) images (Figure 2i, deposited capacity of 5 mAh cm^{-2}) reveal that SFD promotes porous Li deposits and LP57/VC induces dendrites formation (Figure S13). In contrast, the 2D instantaneous Li nucleation with 3D growth behavior enabled by LCCE (Figure 2h) seem to contribute to the denser Li morphologies. The moderately higher exchange current density (compared to LCE-DME) together with a dense Li deposition suggests the effective SEI passivation and subsequent current homogenization.

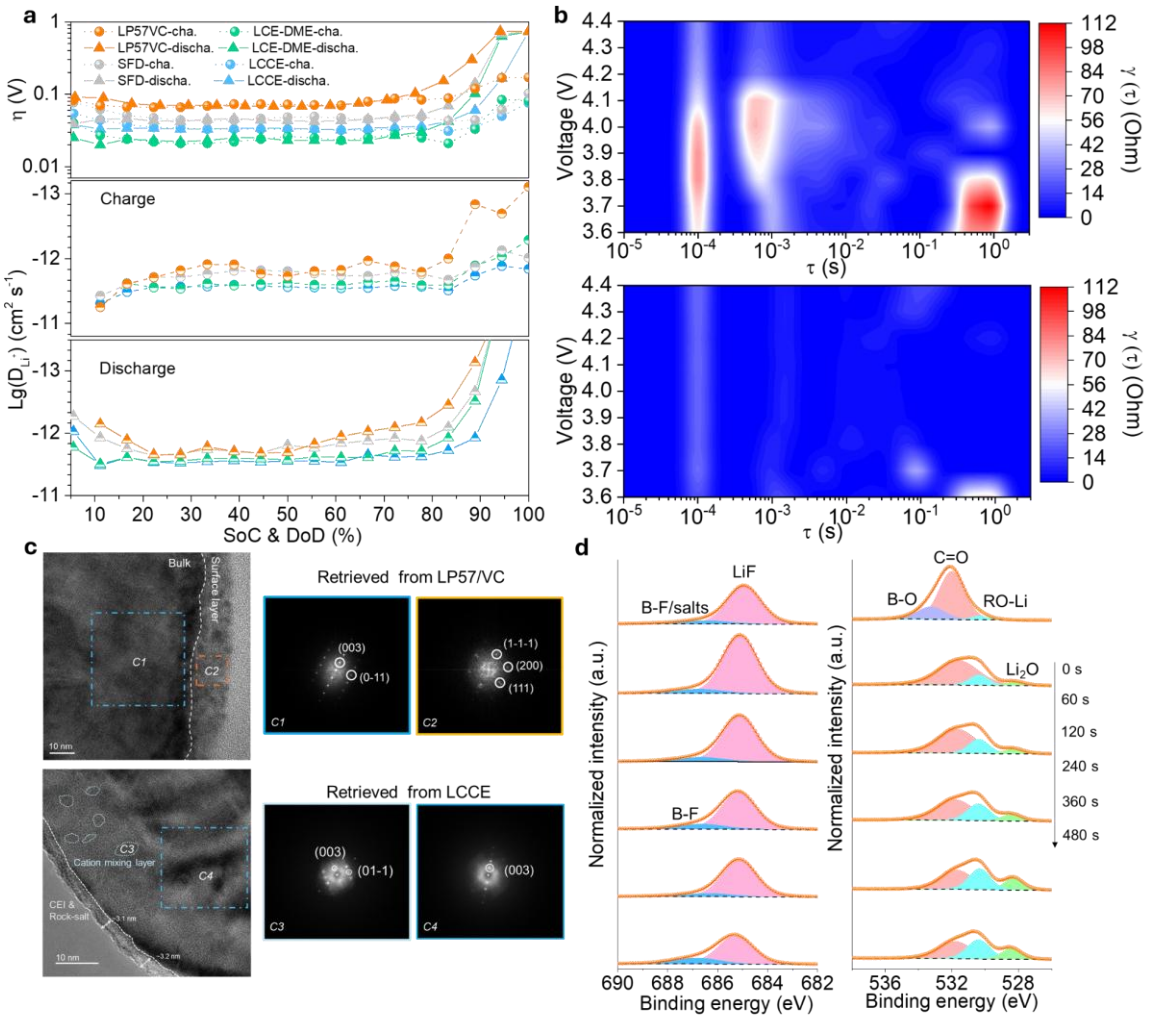


Figure 3. (a) Overpotentials evolution and Li^+ diffusion coefficients versus state/depth of charge/discharge for cells using different electrolytes. (b) Distribution of relaxation times contour plots for cells using LP57/VC and LCCE electrolytes at different states of charge. (c) TEM images of the cycled NMC811 retrieved from LP57/VC and LCCE, scale bar 10 nm. (d) In depth XPS profiles of cycled LMAs retrieved from LCCE-based cells.

In what follows, our cell cycling experiments are carried out with high areal-loading NMC811 cathodes (~4 mAh cm^{-2}) as this is key to achieve high cell level energy density, yet this leads to accelerated degradation. The cells were cycled until their capacity retention drops to 80% (see Figure S14) and were then subjected to electrochemical and post-mortem analyses. As expected, the LCCE outperforms the commercial carbonated electrolyte and other contrast electrolytes, with the longest cell cycling time. After cycling with 80% capacity retention, galvanostatic intermittent titration techniques (GITT) based on the cycled cells (Figure S15) were carried out, which reveal that, compared to the contrast electrolytes, cells using LCCE

electrolyte retain a lower overpotential and the highest Li^+ diffusion coefficients ($D_{Li^+} \approx 2\text{-}4\times10^{-11}$ cm^2 s^{-1}), as plotted in **Figure 3**a, indicative of favorable interfacial kinetics. To further analyses the cell impedance evolution, we conducted electrochemical impedance spectroscopy (EIS) and distribution of relaxation times (DRT) analysis of the cycled cells. In contrast with LP57/VC electrolyte (Figure 3b), the LCCE-based cells display both much lower impedances at (τ) of 10^{-3} and 6×10^{-2}-1.6 s, corresponding to SEI and charge-transfer impedances respectively.[36-38] This difference is also evident in the in situ charge-discharge DRT analysis conducted after the early-stage cycling of the cells (Figure S16), indicating that LCCE exhibits significant advancement in the rapid construction of favorable electrode interfaces. Additionally, the SFD and LCE-DME respectively shows a higher cathode surface impedance growth ($\tau\approx9\times10^{-2}$) and charge-transfer impedances (Figure S17), which is in agreement with their discounted cycling stability.[37]

Then, the cells were disassembled and the cycled electrodes were retrieved for post-mortem analysis. The microstructures of the cycled NMC811 cathodes were examined by transmission electron microscopy (TEM). TEM images of cycled NMC811 reveal a ~3 nm surface reconstruction layer (rock-salt phase plus cathode-electrolyte interphase, CEI) for LCCE, contrasting with >10 nm layers of rock salt phases and thick CEI in LP57/VC (Figure 3c). These results are in agreement with the voltage hold experiments and the increased overpotential and Li^+ transport measured by GITT and EIS/DRT.[39] The LCE-DME and LCCE-cycled cathodes show a similar interfacial layer (Figure S18), but the former seems result in more cation mixing regions.

Next, X-ray photoelectron spectroscopy (XPS) of the cycled LMAs were then conducted. The results show that LMAs cycled with LCCE electrolytes have a higher abundance of LiF on surface layer across all etching depths (Figure 3d, Figure S19). The content of Li_2O increases more evidently in LCCE with prolonged etching time. In addition, organic species (e.g., C=O) and Li-B-O containing compounds were also detected (Figure S20), which are likely to contribute to improving the mechanical resilience and flexibility of the SEI. Conversely, LCE-DME generated SEIs dominated by B-O/Li-B-O species and organic components (Figure S19 and S20),[40, 41] Throughout the depth profile, the LiF content remains lower than that of the SFD and LCCE. Almost no Li_2O is observed as the etching time increases. The inorganic-rich SEI incorporated with a moderate content of organic species in LCCE seems to be essential for maintaining the stability of the LMA. These results and findings also underscore the solvation play an important role in SEI composition. We therefore further investigate differences in solvation and coordination between solvents, ions, and ionic pairs within the investigated

electrolytes.

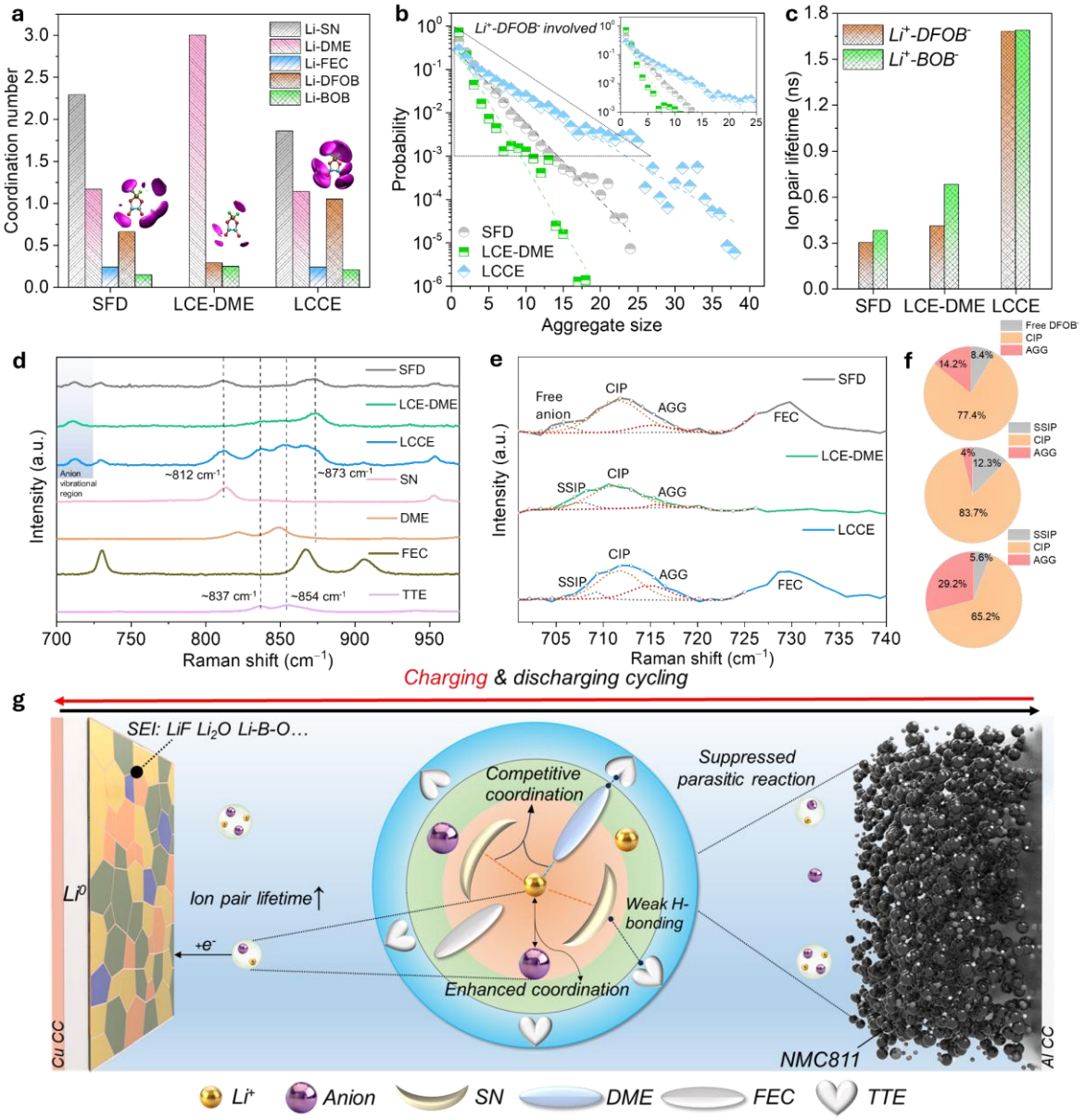


Figure 4. (a) Coordination numbers of Li^+ with solvents/anions within different electrolytes. (b and c) Cluster size distributions and ion-pair lifetimes derived from MD simulations. (d) Raman spectra of different electrolyte and neat solvents. (e) Deconvolution of the anion vibrational regions in the Raman spectra of three electrolytes and (f) the relative proportions of the various clusters obtained, shown from top to bottom are SFD, LCE-DME, and LCCE. (g) Schematic illustration of the mechanism by which the unique solvation structure of LCCE enhances electrode and interfacial compatibility.

MD simulations were employed to elucidate Li^+ interactions with solvent molecules and anions within these electrolytes (snapshots of the MD simulation boxes shown in Figure S21).

Coordination numbers (CN) between Li^+ and solvent/anion species based on RDF analysis (Figure S22) and SDFs between $DFOB^-$ and Li^+ are summarized in **Figure 4**a. In LCE-DME, the Li^+-DME, the CN reaches 3.00, which is the highest among all electrolytes studied here. This value decreases significantly to 1.17 in SFD due to less proportion of DME and competitive coordination from the cyano in SN, which attenuate Li^+-DME interactions. The diminished Li^+-SN CN (2.29) in SFD compared to SN-borate eutectic electrolytes (3.30, Figure S4) corroborates competitive coordination mechanism, given the minimal Li^+-FEC coordination (CN: 0.24). Upon addition of TTE (i.e. LCCE electrolyte), the Li^+-SN coordination (CN: 1.86) decreases relative to SFD, aligning with prior findings on intermolecular hydrogen bonding between TTE and SN. Concurrently, LCCE exhibits the highest Li^+-$DFOB^-$ coordination (CN: 1.05) and intermediate Li^+-BOB^- coordination (CN: 0.21 vs. 0.15 in SFD and 0.25 in LCE-DME) among investigated electrolytes. These coordination environments are further supported by the probability distributions of Li^+ coordination with each electrolyte component (Figure S23). In addition, the Li^+-BOB^- interaction in SDF and LCCE occurs primarily through coordination with the carbonyl oxygen, whereas in LCE-DME, Li^+ also interacts with the B-O oxygens (Figure S24). The multiple peaks observed in the Li-BOB RDF (Figure S22) suggest the presence of multiple coordination sites, which may be mediated by the strong Li^+-DME coordination (Figure S23). Higher concentrations of Li ions surrounding $DFOB^-$ are also observed in LCCE compared to the other electrolytes (inset Figure 4a). The presence of TTE may balances the competitive coordination between Li^+ and SN/DME and enhances Li^+-$DFOB^-$ interaction even TTE not directly participating in the solvation of Li^+ as shown by RDF results for LCE-DME and LCCE.[42, 43] The synergistic effect between TTE and the competitive solvent composition seem to lead to larger Li^+-$DFOB^-$ aggregates (AGGs) in LCCE compared to LCE-DME and SFD (Figure 4b). Ion pair lifetime analysis (Figure 4c) reveals that LCCE possesses the longest Li^+-$DFOB^-$ contacted ion pair (CIP) lifetime. This AGG-enriched solvation architecture, coupled with prolonged CIP lifetimes, has been confirmed to enhance anion contribution to the SEI and improve cycling stability.[44-46]

To experimentally understand solvation environments within investigated electrolytes, the Raman spectra of electrolytes and their neat solvents were collected and presented in Figure 4d. In all electrolytes, the characteristic peaks of pure DME (~823 and 850 cm^{-1}) disappear or shift, while a new peak emerges at ~873 cm^{-1}, which indicate that DME participates in solvation for all three electrolytes.[47] Notably, the coordinated DME peaks in SFD and LCCE exhibit lower intensity and broader profiles compared to LCE-DME, suggesting that the synergistic solvation effect of SN (corresponding to the ~812 cm^{-1} peak) interferes with or attenuates the strong

solvation capability of DME.[48] Due to a high solvent-to-diluent ratio and stronger solvation capability of DME compared to TTE, the characteristic peaks associated with TTE are nearly undetectable in LCE-DME, whereas distinct TTE-related peaks are observed in LCCE. This phenomenon arises from the reduced DME content and weaker binding affinity between SN and TTE. The weakly bound or free TTE molecules in LCCE may contribute to maintaining low bulk viscosity and providing fluorine for interphase formation. We then deconvoluted the anion ($DFOB^-$) vibrational regions in the Raman spectra of the three electrolytes and analyzed the proportions of anion-related clusters, as shown in Figure 4e and f. Among the three electrolytes, LCCE exhibits the lowest SSIP fraction (5.6%) and the highest AGG fraction (29.2%), indicating a high abundance of $DFOB^-$ around Li^+ and stronger Li^+-anion interactions.[49-51] Raman spectra of LCCEs with different SN/DME molar ratios were also investigated (Figure S25). As the SN increases, the anion-related Raman peaks shift overall to higher wavenumbers. Deconvolution further reveals that the proportion of free anions or SSIPs in the electrolyte clusters decreases, while AGGs emerge and their proportion increases. This solvation cluster evolution would enable the anions to be more preferentially reduced and efficiently participated in forming and constituting the critical interfacial layers, thereby mitigating the crosstalk between the electrodes and their respective degradation (Figure 4g), which helps prolong the cell lifespan.

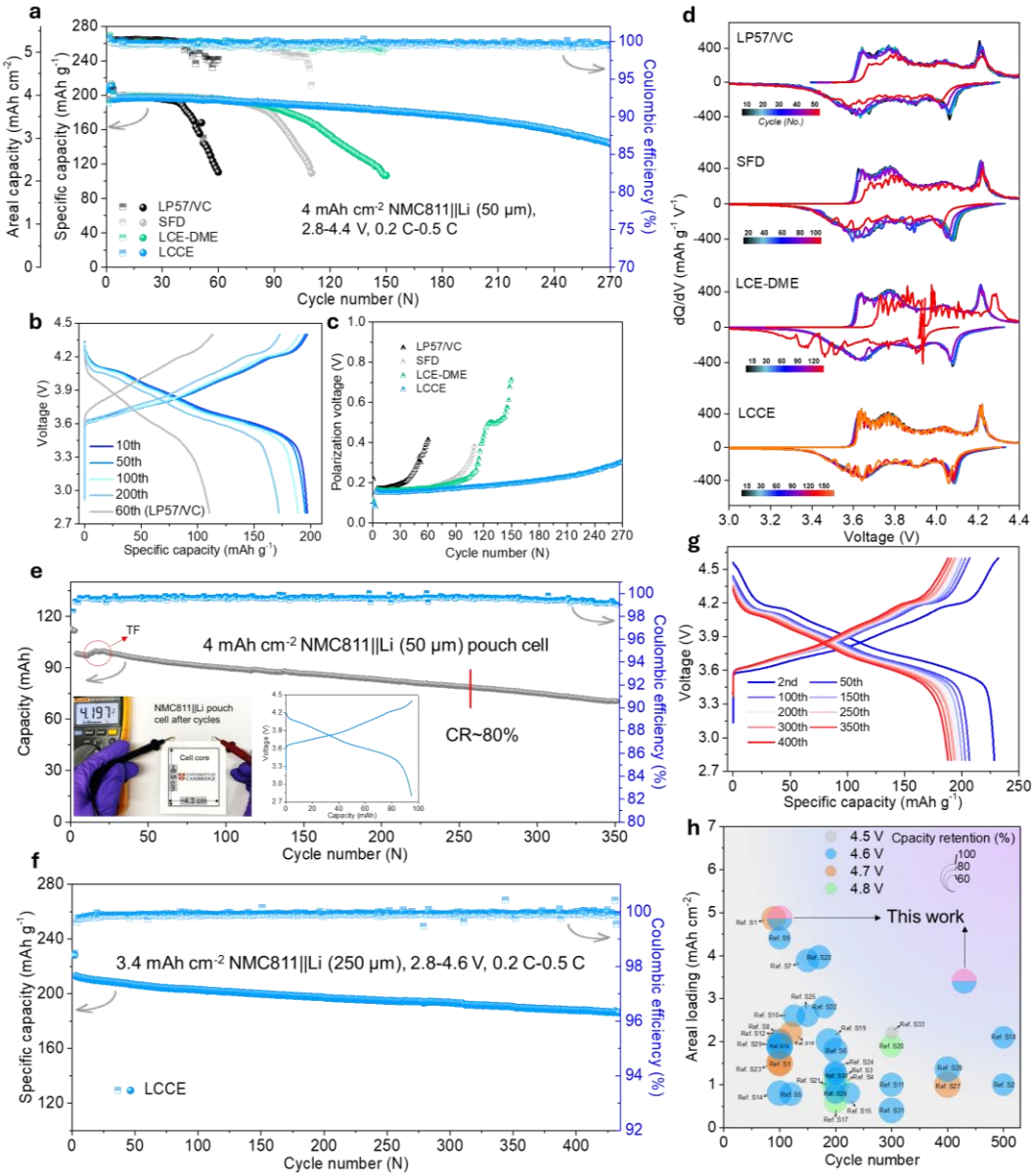


Figure 5. (a) Cycling performance of NMC811||Li cells with different electrolytes under low N/P ratio conditions. (b) Typical charge/discharge profiles for cells using LCCE and LP57/VC. (c) Polarization voltages of cells with different electrolytes as a function of cycle number. (d) Differential capacity (dQ/dV) profiles of cells at typical cycles using different electrolytes. (e) Cycling performance of the pouch cell using LCCE. (f) Cycling performance and (g) typical charge/discharge curve of cell using LCCE at upper cutoff voltage of 4.6 V. (h) Bubble plot of the performance of high-voltage high-nickel (Ni%>80) Li metal batteries based on cycle number, capacity retention, and cathode loading.

We subsequently evaluated the cycling performance of reference electrolytes and LCCE electrolytes using a 50 μm thick LMA, which with high areal capacity cathodes (4 mAh cm^{-2})

corresponds to a low N/P ratio of ~2.5. Under this harsh operating condition, the LCCE-based cells sustained 80% capacity retention over 247 cycles, which is a five-fold improvement compared to cells with carbonate-based electrolytes (49 cycles) and over two-fold for other contrast electrolytes (SFD: 96 cycles; LCE: 117 cycles; **Figure 5**a). Compared to these references, we observe less polarization in cells using LCCE during cycling (Figure 5b and c). The reduction in impedance growth with the least variation of high-voltage H2-H3 phase transition peaks are also observed from differential capacity (dQ/dV) profiles (Figure 5d).[52] The compatibility with larger format cells using LCCE was validated in pouch cells under the same conditions as above (E/C ratio = 3 g Ah^{-1}, Figure 5e), which achieve 80% capacity retention over 258 cycles (71.7% after 350 cycles).

We further raised the upper cutoff voltage of the cell tests to 4.6 V. The cells incorporating a high-loading cathode (3.4 mAh cm^{-2}) with LCCE delivered a stable cycling performance for 430 cycles at a discharge rate of 0.5 C, retaining a capacity retention of 87.5% (Figure 5f and g). When the cathode loading was further increased to 4.86 mAh cm^{-2} and the LMA thickness was reduced to 100 μm, LCCE still enabled a capacity retention of 90% after 100 cycles (Figure S26). Compared with the reported cycling performance of high-voltage (≥4.6 V) LMB based on high-loading Ni-rich cathodes (Ni%≥80), the LCCE electrolyte strategy exhibits outstanding competitiveness (Figure 5h and Table S2). Elevating the upper cut-off voltage inevitably exacerbates TM dissolution and structural degradation of NMC811. Furthermore, we conducted postmortem analysis, including inductively coupled plasma mass spectrometry (ICP-MS), TEM, and X-ray diffraction (XRD) on the retrieved cell components cycled at 4.6 V (Figure S27-29). After cycling, the LCCE cells exhibited less TM dissolution compared to LP57/VC. A more uniform interphase layer was observed on NMC811, the integrity within its bulk was also well maintained, demonstrating superior compatibility of LCCE with Ni-rich cathodes at high-voltage operation.

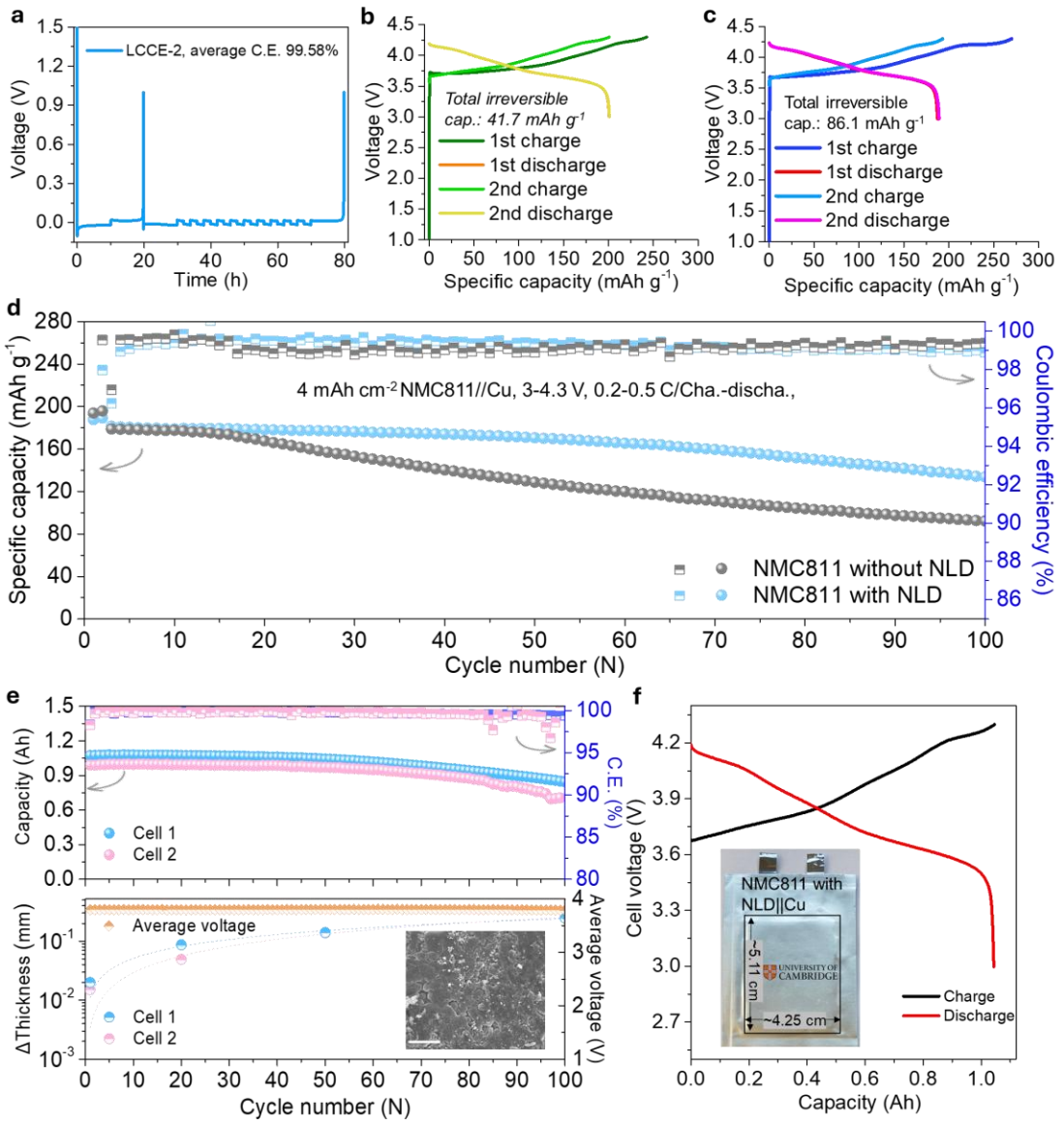


Figure 6. (a) Average CE of the modified LCCE-2 based on Aurbach method. (b and c) Charge/discharge curves of anode-free cells with and without NLD during initial two cycles. (d) Cycling performance of anode-free cell architecture integrating NLD and LCCE-2. (e) Cycling performance, corresponding thickness (after discharging) and average voltage change of the anode-free pouch cells, the inset shows the redeposited Li after long-term cycling, scale bar is 20 μm. (f) Typical charge and discharge curves of anode-free pouch cell.

Finally, we test the performance of our electrolyte in more aggressive cell configurations, anode-free (N/P=0) cells. Given the relatively low Aurbach CE of the above mentioned LCCE (attributed to the high dissociation energy of the borate salt), we adjusted the salt for anode-free cells through using more readily dissociating, fluorine-rich LiTFSI and LiFSI, along with trace amount (~4 wt.% vs. DME) of $LiNO_3$ additives (denoted as LCCE-2). Notably, although the

elevated DME ratio in LCCE-2 leads to an increased proportion of SSIPs, the proportion of AGGs is not decreased too much, and the larger AGG+ is observed (Figure S30nd S31). This suggests that the remained competitive coordination between SN and DME can still allow anions to penetrate into the inner solvation sheath. This modification significantly enhances Li platting/stripping reversibility, achieving an Aurbach CE of 99.58% (**Figure 6**a), which is on par with state-of-the-art electrolytes. As expected, the cycling stability of the anode-free with LCCE-2 outperforms the one with LCCE (Figure S32).

We also carried out anode-free cell test using LCCE-2 and a biphasic nanocomposite lithium donor (NLD) comprising Li_3N and $Li_{6.4}La_3Zr_{1.4}Ta_{0.6}O_{12}$ (LLZTO), which is mixed with the cathode (Figure S33). Li_3N was selected for the NLD due to its high capacity, which minimizes its impact on the overall energy density of the battery. The use of a Li inventory donor in high-loading electrodes poses a challenge: the resistive by-products and voids formed after consumption hinder Li^+ diffusion, can lead to rapid capacity fade. Therefore, we embed Li_3N particles in LLZTO (Figure S34) to preserve ion transport through LLZTO after Li_3N depletion, thus minimizing subsequent performance loss (see Figure S35). Incorporating 6 wt% NLD, of which 2 wt% is active Li_3N, elevates the irreversible capacity by ~106.5% during the first two cycles compared to the reference NMC811 electrode (Figure 6b and c). The Li inventory supplied by NLD enables anode-free cells to achieve ~74.6% capacity retention over 100 cycles with a voltage range from 2.8 to 4.3 V, substantially outperforming NLD-free systems (Figure S36 and S37). At elevated cycling rates (0.2 C charge and 0.5 C discharge), the cells utilizing LCCE-2 paired with NLD retain ~73.7% of their capacity after 100 cycles (Figure 6d), which outperforms the anode-free cells with only LCCE-2 as well those with NLD but employing a classic LiFSI-DME-TTE (1:1.2:3 in molar ratio) electrolyte or LCE-DME-2 (salts and solvent/diluents ratio are same with those of LCCE-2) (Figure S38 and S39). Finally, the above strategy was further validated in Ah-level (6 layers double-side coated cathodes) zigzag-stacked pouch cells (Table S3). Using high cathode loading (4.3-4.4 mAh cm^{-2}) and lower E/C ratio (2.1 g Ah^{-1}), one pouch cell delivers 1.074 Ah at 0.5 C discharging rate with high average voltage and small polarization (Figure 6e and f). After 100 cycles, it retains ~78.7% of its initial capacity together with a cell thickness change of 0.246 mm. The SEM image of the redeposited Li after long-term cycling reveals a dense and chunky morphology (inset in Figure 6e), which is corelated with the sustained performance and inhibited inactive Li accumulation. These results collectively validate the potential of LCCE electrolytes combined with NLD for anode-free batteries.

3. Conclusion

In summary, achieving ultra-high energy density LMAs demands high energy density cathodes operating in their full voltage window. For NMC811, this leads to parasitic reaction and TM dissolution processes that poison the LMA SEI. We employ a combination of SN/FEC-DME cosolvent-TTE diluent and dual-borate salts, leading to less gas evolution and TM dissolution which we verify by leakage current, in situ DEMS, ICP-MS, GITT, in situ DRT, and TEM analysis. Our investigation reveals that anode stability is improved by SN and DME both engaging in competitive Li^+ coordination. Coupled with the intermolecular hydrogen bonding between TTE and these solvents, this competition enhances the interaction between Li^+ and anions, increasing the probability of AGG formation and prolonging the lifetime of CIPs, which corroborate the observed LiF-rich SEI. We demonstrate the viability of this electrolyte in pouch cells with high areal cathode capacity (4 mAh cm^{-2}) and thin LMA (50 μm). These cells reach capacity retention of 80% over 250 cycles. Furthermore, this electrolyte enables the LMBs to stably cycle over 430 cycles with 87.5% capacity retention even under the high-voltage (4.6 V) and high-loading cathode conditions. Finally, the synergy between LCCE and a biphasic NLD allows for a 1.07 Ah format anode-free pouch cell with a capacity retention of 78.7% over 100 cycles. These findings underscore the importance of LMA and anode-free battery electrolyte development that balance both the reversibility of LMA and suppression of cathode surface reaction mechanisms.

Acknowledgements

This research was funded by European Research Council (ERC) Consolidator Grant (MIGHTY 866005) and the Faraday Institution (Degradation FIRG024, FIRG060) and used the Michael Computing Facility funded by the Faraday Institution (FIRG019).

Conflicts of interest

The authors declare no conflicts of interest.

Data Availability Statement

The data that support the findings of this study are available from the corresponding author upon reasonable request.

Received: ((will be filled in by the editorial staff))
Revised: ((will be filled in by the editorial staff))
Published online: ((will be filled in by the editorial staff))

References

1. M. Armand and J. M. Tarascon, "Building Better Batteries," *Nature* **451** (2008): 652–657, https://doi.org/10.1038/451652a.
2. S. Chu, Y. Cui, and N. Liu, "The Path towards Sustainable Energy," *Nature Materials* **16** (2017): 16–22, https://doi.org/10.1038/nmat4834.
3. M. Li, J. Lu, Z. Chen, and K. Amine, "30 Years of Lithium-Ion Batteries," *Advanced Materials* **30** (2018): e1800561, https://doi.org/10.1002/adma.201800561.
4. G. Z. Yang, J. Bellingham, P. E. Dupont, P. Fischer, L. Floridi, R. Full, N. Jacobstein, V. Kumar, M. McNutt, R. Merrifield, B. J. Nelson, B. Scassellati, M. Taddeo, R. Taylor, M. Veloso, Z. L. Wang, and R. Wood, "The Grand Challenges of Science Robotics," *Science Robotics* **3** (2018): eaar7650, https://doi.org/10.1126/scirobotics.aar7650.
5. V. Viswanathan, A. H. Epstein, Y. M. Chiang, E. Takeuchi, M. Bradley, J. Langford, and M. Winter, "The Challenges and Opportunities of Battery-Powered Flight," *Nature* **601** (2022): 519–525, https://doi.org/10.1038/s41586-021-04139-1.
6. J. W. Choi and D. Aurbach, "Promise and Reality of Post-Lithium-Ion Batteries with High Energy Densities," *Nature Reviews Materials* **1** (2016): 16013, https://doi.org/10.1038/natrevmats.2016.13.
7. D. Lin, Y. Liu, and Y. Cui, "Reviving the Lithium Metal Anode for High-Energy Batteries," *Nature Nanotechnology* **12** (2017): 194–206, https://doi.org/10.1038/nnano.2017.16.
8. F. Duffner, N. Kronemeyer, J. Tübke, J. Leker, M. Winter, and R. Schmuch, "Post-Lithium-Ion Battery Cell Production and Its Compatibility with Lithium-Ion Cell Production Infrastructure," *Nature Energy* **6** (2021): 123–134, https://doi.org/10.1038/s41560-020-00748-8.
9. W. Li, E. M. Erickson, and A. Manthiram, "High-Nickel Layered Oxide Cathodes for Lithium-Based Automotive Batteries," *Nature Energy* **5** (2020): 26–34, https://doi.org/10.1038/s41560-019-0513-0.

10. J. Liu, Z. Bao, Y. Cui, E. J. Dufek, J. B. Goodenough, P. Khalifah, Q. Li, B. Y. Liaw, P. Liu, A. Manthiram, Y. S. Meng, V. R. Subramanian, M. F. Toney, V. V. Viswanathan, M. S. Whittingham, J. Xiao, W. Xu, J. Yang, X.-Q. Yang, and J.-G. Zhang, "Pathways for Practical High-Energy Long-Cycling Lithium Metal Batteries," *Nature Energy* **4** (2019): 180–186, https://doi.org/10.1038/s41560-019-0338-x.
11. M. He, L. G. Hector, F. Dai, F. Xu, S. Kolluri, N. Hardin, and M. Cai, "Industry Needs for Practical Lithium-Metal Battery Designs in Electric Vehicles," *Nature Energy* **9** (2024): 1199–1205, https://doi.org/10.1038/s41560-024-01624-5.
12. X. Fan and C. Wang, "High-Voltage Liquid Electrolytes for Li Batteries: Progress and Perspectives," *Chemical Society Reviews* **50** (2021): 10486–10566, https://doi.org/10.1039/d1cs00450f.
13. K. Xu, "Electrolytes and Interphases in Li-Ion Batteries and Beyond," *Chemical Reviews* **114** (2014): 11503–11618, https://doi.org/10.1021/cr500003w.
14. Y. Zhang, Y. Katayama, R. Tatara, L. Giordano, Y. Yu, D. Fraggedakis, J. G. Sun, F. Maglia, R. Jung, M. Z. Bazant, and Y. Shao-Horn, "Revealing Electrolyte Oxidation via Carbonate Dehydrogenation on Ni-Based Oxides in Li-Ion Batteries by in Situ Fourier Transform Infrared Spectroscopy," *Energy & Environmental Science* **13** (2020): 183–199, https://doi.org/10.1039/c9ee02543j.
15. C. Wang, L. Xing, J. Vatamanu, Z. Chen, G. Lan, W. Li, and K. Xu, "Overlooked Electrolyte Destabilization by Manganese (II) in Lithium-Ion Batteries," *Nature Communications* **10** (2019): 3423, https://doi.org/10.1038/s41467-019-11439-8.
16. W. M. Dose, I. Temprano, J. P. Allen, E. Bjorklund, C. A. O'Keefe, W. Li, B. L. Mehdi, R. S. Weatherup, M. F. L. De Volder, and C. P. Grey, "Electrolyte Reactivity at the Charged Ni-Rich Cathode Interface and Degradation in Li-Ion Batteries," *ACS Applied Materials & Interfaces* **14** (2022): 13206–13222, https://doi.org/10.1021/acsami.1c22812.
17. S. Chen, J. Zheng, D. Mei, K. S. Han, M. H. Engelhard, W. Zhao, W. Xu, J. Liu, and J. G. Zhang, "High-Voltage Lithium-Metal Batteries Enabled by Localized High-Concentration Electrolytes," *Advanced Materials* **30** (2018): e1706102, https://doi.org/10.1002/adma.201706102.
18. X. Ren, L. Zou, X. Cao, M. H. Engelhard, W. Liu, S. D. Burton, H. Lee, C. Niu, B. E. Matthews, Z. Zhu, C. Wang, B. W. Arey, J. Xiao, J. Liu, J.-G. Zhang, and W. Xu, "Enabling High-Voltage Lithium-Metal Batteries under Practical Conditions," *Joule* **3** (2019): 1662–1676, https://doi.org/10.1016/j.joule.2019.05.006.
19. X. Cao, X. Ren, L. Zou, M. H. Engelhard, W. Huang, H. Wang, B. E. Matthews, H. Lee,

C. Niu, B. W. Arey, Y. Cui, C. Wang, J. Xiao, J. Liu, W. Xu, and J.-G. Zhang, "Monolithic Solid–Electrolyte Interphases Formed in Fluorinated Orthoformate-Based Electrolytes Minimize Li Depletion and Pulverization," *Nature Energy* **4** (2019): 796–805, https://doi.org/10.1038/s41560-019-0464-5.

20. Z. Yu, H. Wang, X. Kong, W. Huang, Y. Tsao, D. G. Mackanic, K. Wang, X. Wang, W. Huang, S. Choudhury, Y. Zheng, C. V. Amanchukwu, S. T. Hung, Y. Ma, E. G. Lomeli, J. Qin, Y. Cui, and Z. Bao, "Molecular Design for Electrolyte Solvents Enabling Energy-Dense and Long-Cycling Lithium Metal Batteries," *Nature Energy* **5** (2020): 526–533, https://doi.org/10.1038/s41560-020-0634-5.
21. Z. Yu, P. E. Rudnicki, Z. Zhang, Z. Huang, H. Celik, S. T. Oyakhire, Y. Chen, X. Kong, S. C. Kim, X. Xiao, H. Wang, Y. Zheng, G. A. Kamat, M. S. Kim, S. F. Bent, J. Qin, Y. Cui, and Z. Bao, "Rational Solvent Molecule Tuning for High-Performance Lithium Metal Battery Electrolytes," *Nature Energy* **7** (2022): 94–106, https://doi.org/10.1038/s41560-021-00962-y.
22. J. Zhang, Q. Li, Y. Zeng, Z. Tang, D. Sun, D. Huang, Y. Tang, and H. Wang, "Weakly Solvating Cyclic Ether Electrolyte for High-Voltage Lithium Metal Batteries," *ACS Energy Letters* **8** (2023): 1752–1761, https://doi.org/10.1021/acsenergylett.3c00181.
23. J. Sun, B. Wen, Y. Li, H. Wang, and M. De Volder, "Improving Cycle Life of Ni-Rich Li-Ion Battery Cathodes by Using Compartmentalized Anode and Cathode Electrolytes," *Small* **21** (2025): e2410149, https://doi.org/10.1002/smll.202410149.
24. Q. Zhang, K. Liu, F. Ding, W. Li, X. Liu, and J. Zhang, "Enhancing the High Voltage Interface Compatibility of $LiNi_{0.5}Co_{0.2}Mn_{0.3}O_2$ in the Succinonitrile-Based Electrolyte," *Electrochimica Acta* **298** (2019): 818–826, https://doi.org/10.1016/j.electacta.2018.12.104.
25. Z. Hu, F. Xian, Z. Guo, C. Lu, X. Du, X. Cheng, S. Zhang, S. Dong, G. Cui, and L. Chen, "Nonflammable Nitrile Deep Eutectic Electrolyte Enables High-Voltage Lithium Metal Batteries," *Chemistry of Materials* **32** (2020): 3405–3413, https://doi.org/10.1021/acs.chemmater.9b05003.
26. J. Cha, J.-G. Han, J. Hwang, J. Cho, and N.-S. Choi, "Mechanisms for Electrochemical Performance Enhancement by the Salt-Type Electrolyte Additive, Lithium Difluoro(oxalato)borate, in High-Voltage Lithium-Ion Batteries," *Journal of Power Sources* **357** (2017): 97–106, https://doi.org/10.1016/j.jpowsour.2017.04.094.
27. H. Xiang, P. Shi, P. Bhattacharya, X. Chen, D. Mei, M. E. Bowden, J. Zheng, J.-G. Zhang, and W. Xu, "Mechanisms for Electrochemical Performance Enhancement by the Salt-Type Electrolyte Additive, Lithium Difluoro(oxalato)borate, in High-Voltage Lithium-Ion

Batteries," *Journal of Power Sources* **318** (2016): 170–177, https://doi.org/10.1016/j.jpowsour.2017.04.094.

28. G. Xu, X. Shangguan, S. Dong, X. Zhou, and G. Cui, "Formulation of Blended-Lithium-Salt Electrolytes for Lithium Batteries," *Angewandte Chemie International Edition* **59** (2020): 3400–3415, https://doi.org/10.1002/anie.201906494.
29. S. Wang, L. Zhang, Z. Hu, B. Zhang, N. Li, Y. B. Tong, D. Cao, X. Zheng, W. Y. Lai, Z. Jin, F. Wu, and Q. Wang, "Intrinsic Structural and Coordination Chemistry Insights of Li Salts in Rechargeable Lithium Batteries," *Advanced Materials* **37** (2025): e2420428, https://doi.org/10.1002/adma.202420428.
30. M. Qin, Z. Zeng, Q. Wu, X. Liu, Q. Liu, S. Cheng, and J. Xie, "4-Fluorobenzyl Cyanide, a Sterically-Hindered Solvent Expediting Interfacial Kinetics in Lithium-Ion Batteries," *Chemical Science* **15** (2024): 6106–6114, https://doi.org/10.1039/d4sc00013g.
31. C. Che, R. Zhang, Y. Li, H. Li, S. Li, J. Qian, Y. Gong, H. Li, Y. Bai, F. Wu, and C. Wu, "Fundamental Chemistry and Functional Mechanisms of Nitrile-Based Electrolyte in Advanced Battery Systems," *Advanced Materials* **37** (2025): e2506504, https://doi.org/10.1002/adma.202506504.
32. A. Luzar and D. Chandler, "Hydrogen-Bond Kinetics in Liquid Water," *Nature* **379** (1996): 55–57, https://doi.org/10.1038/379055a0.
33. W. M. Dose, W. Li, I. Temprano, C. A. O'Keefe, B. L. Mehdi, M. F. L. De Volder, and C. P. Grey, "Onset Potential for Electrolyte Oxidation and Ni-Rich Cathode Degradation in Lithium-Ion Batteries," *ACS Energy Letters* **7** (2022): 3524–3530, https://doi.org/10.1021/acsenergylett.2c01722.
34. B. L. D. Rinkel, J. P. Vivek, N. Garcia-Araez, and C. P. Grey, "Two Electrolyte Decomposition Pathways at Nickel-Rich Cathode Surfaces in Lithium-Ion Batteries," *Energy & Environmental Science* **15** (2022): 3416–3438, https://doi.org/10.1039/d1ee04053g.
35. Y. Liu, X. Xu, M. Sadd, O. O. Kapitanova, V. A. Krivchenko, J. Ban, J. Wang, X. Jiao, Z. Song, J. Song, S. Xiong, and A. Matic, "Insight into the Critical Role of Exchange Current Density on Electrodeposition Behavior of Lithium Metal," *Advanced Science* **8** (2021): 2003301, https://doi.org/10.1002/advs.202003301.
36. P. Iurilli, C. Brivio, and V. Wood, "Detection of Lithium-Ion Cells' Degradation through Deconvolution of Electrochemical Impedance Spectroscopy with Distribution of Relaxation Time," *Energy Technology* **10** (2022): 2200547, https://doi.org/10.1002/ente.202200547.

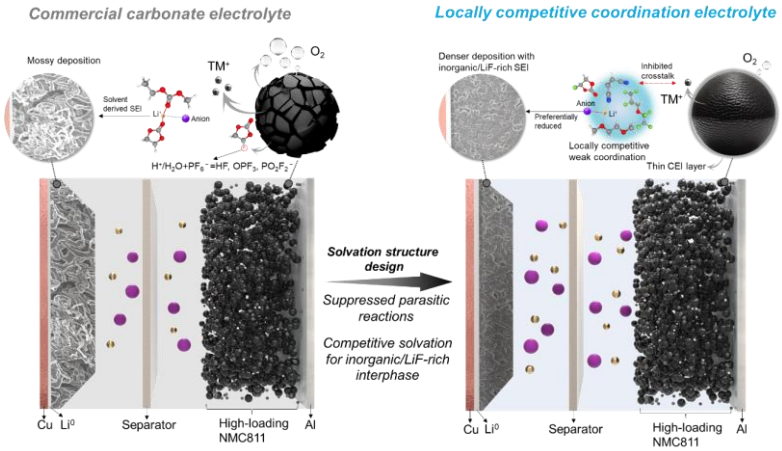
37. M. Leal de Souza and M. Morcrette, "Coupling Differential Voltage Analysis and Distribution of Relaxation Times I: Evaluating the Impact of NMC811 Coating in the Degradation of NMC811/Gr Cells," *Journal of Power Sources* **645** (2025): 237184, https://doi.org/10.1016/j.jpowsour.2025.237184.
38. Y. Lu, C.-Z. Zhao, J.-Q. Huang, and Q. Zhang, "The Timescale Identification Decoupling Complicated Kinetic Processes in Lithium Batteries," *Joule* **6** (2022): 1172–1198, https://doi.org/10.1016/j.joule.2022.05.005.
39. C. Xu, K. Marker, J. Lee, A. Mahadevegowda, P. J. Reeves, S. J. Day, M. F. Groh, S. P. Emge, C. Ducati, B. Layla Mehdi, C. C. Tang, and C. P. Grey, "Bulk Fatigue Induced by Surface Reconstruction in Layered Ni-Rich Cathodes for Li-Ion Batteries," *Nature Materials* **20** (2021): 84–92, https://doi.org/10.1038/s41563-020-0767-8.
40. Y. Yang, X. Wang, J. Zhu, L. Tan, N. Li, Y. Chen, L. Wang, Z. Liu, X. Yao, X. Wang, X. Ji, and Y. Zhu, "Dilute Electrolytes with Fluorine-Free Ether Solvents for 4.5 V Lithium Metal Batteries," *Angewandte Chemie International Edition* **63** (2024): e202409193, https://doi.org/10.1002/anie.202409193.
41. S. Li, Q. Liu, W. Zhang, L. Fan, X. Wang, X. Wang, Z. Shen, X. Zang, Y. Zhao, F. Ma, and Y. Lu, "High-Efficacy and Polymeric Solid-Electrolyte Interphase for Closely Packed Li Electrodeposition," *Advanced Science* **8** (2021): 2003240, https://doi.org/10.1002/advs.202003240.
42. C. M. Efaw, Q. Wu, N. Gao, Y. Zhang, H. Zhu, K. Gering, M. F. Hurley, H. Xiong, E. Hu, X. Cao, W. Xu, J. G. Zhang, E. J. Dufek, J. Xiao, X. Q. Yang, J. Liu, Y. Qi, and B. Li, "Localized High-Concentration Electrolytes Get More Localized through Micelle-Like Structures," *Nature Materials* **22** (2023): 1531–1539, https://doi.org/10.1038/s41563-023-01700-3.
43. X. Cao, P. Gao, X. Ren, L. Zou, M. H. Engelhard, B. E. Matthews, J. Hu, C. Niu, D. Liu, B. W. Arey, C. Wang, J. Xiao, J. Liu, W. Xu, and J. G. Zhang, "Effects of Fluorinated Solvents on Electrolyte Solvation Structures and Electrode/Electrolyte Interphases for Lithium Metal Batteries," *Proceedings of the National Academy of Sciences of the United States of America* **118** (2021): e2020357118, https://doi.org/10.1073/pnas.2020357118.
44. S. Liu, X. Ji, N. Piao, J. Chen, N. Eidson, J. Xu, P. Wang, L. Chen, J. Zhang, T. Deng, S. Hou, T. Jin, H. Wan, J. Li, J. Tu, and C. Wang, "An Inorganic-Rich Solid Electrolyte Interphase for Advanced Lithium-Metal Batteries in Carbonate Electrolytes," *Angewandte Chemie International Edition* **60** (2021): 3661–3671, https://doi.org/10.1002/ange.202012005.

45. S. Ilic, S. N. Lavan, and J. G. Connell, “Anion-Derived Contact Ion Pairing as a Unifying Principle for Electrolyte Design,” *Chem* **10** (2024): 2987–3007, https://doi.org/10.1016/j.chempr.2024.07.031.
46. A. M. Li, O. Borodin, T. P. Pollard, W. Zhang, N. Zhang, S. Tan, F. Chen, C. Jayawardana, B. L. Lucht, E. Hu, X. Q. Yang, and C. Wang, “Methylation Enables the Use of Fluorine-Free Ether Electrolytes in High-Voltage Lithium Metal Batteries,” *Nature Chemistry* **16** (2024): 922–929, https://doi.org/10.1038/s41557-024-01497-x.
47. Q. Sun, Z. Cao, Z. Ma, J. Zhang, W. Wahyudi, G. Liu, H. Cheng, T. Cai, E. Xie, L. Cavallo, Q. Li, and J. Ming, “Interfacial and Interphasial Chemistry of Electrolyte Components to Invoke High-Performance Antimony Anodes and Non-Flammable Lithium-Ion Batteries,” *Advanced Functional Materials* **33** (2023): 2210292, https://doi.org/10.1002/adfm.202210292.
48. M. Suleman, Y. Kumar, and S. A. Hashmi, “Structural and Electrochemical Properties of Succinonitrile-Based Gel Polymer Electrolytes: Role of Ionic Liquid Addition,” *The Journal of Physical Chemistry B* **117** (2013): 7436–7443, https://doi.org/10.1021/jp312358x.
49. S.-D. Han, O. Borodin, J. L. Allen, D. M. Seo, D. W. McOwen, S.-H. Yun, and W. A. Henderson, “Electrolyte Solvation and Ionic Association IV. Acetonitrile-Lithium Difluoro(oxalato)borate (LiDFOB) Mixtures,” *Journal of The Electrochemical Society* **160** (2013): A2100–A2110, https://doi.org/10.1149/2.094309jes.
50. P. Liang, J. Li, Y. Dong, Z. Wang, G. Ding, K. Liu, L. Xue, and F. Cheng, “Modulating Interfacial Solvation via Ion Dipole Interactions for Low-Temperature and High-Voltage Lithium Batteries,” *Angewandte Chemie International Edition* **64** (2025): e202415853, https://doi.org/10.1002/anie.202415853.
51. M. Li, H. An, Y. Song, Q. Liu, J. Wang, H. Huo, S. Lou, and J. Wang, “Ion−Dipole-Interaction-Induced Encapsulation of Free Residual Solvent for Long-Cycle Solid-State Lithium Metal Batteries," *Journal of the American Chemical Society* **145** (2023): 25632–25642, https://doi.org/10.1021/jacs.3c07482.
52. P. J. West, C. D. Quilty, Z. Wang, S. N. Ehrlich, L. Ma, C. Jaye, D. A. Fischer, X. Tong, A. M. Kiss, E. S. Takeuchi, A. C. Marschilok, K. J. Takeuchi, and D. C. Bock, “Degradation in Ni-Rich $LiNi_{1-x-y}Mn_xCo_yO_2$/Graphite Batteries: Impact of Charge Voltage and Ni Content,” *The Journal of Physical Chemistry C* **127** (2023): 7054–7070, https://doi.org/10.1021/acs.jpcc.2c08971.

Supporting Information

Additional supporting information can be found online in the Supporting Information section.

Locally Competitive Coordination Electrolyte for High-Voltage Lithium-Metal Batteries with Ni-Rich Cathodes



Simultaneously realizing enhanced compatibilities of Ni-rich cathode and Li anode via locally competitive coordination electrolyte.